

Explicit IMF B_y -effect maximizes at subauroral latitudes (Dedicated to the memory of Eigil Friis-Christensen)

L. Holappa^{1,2,3}, N. Gopalswamy² and K. Mursula¹

¹ReSoLVE Centre of Excellence, Space Physics Research Unit, University of Oulu, Oulu, Finland

²NASA Goddard Space Flight Center, Greenbelt, MD, USA

³Catholic University of America, Washington, DC, USA

Key Points:

- IMF B_y -component is an explicit driver of geomagnetic activity, with the largest effect at subauroral latitudes
- B_y -effect increases for strong solar wind driving and for winter conditions
- Maximum B_y -effect is 20% for all solar wind and 40% for CMEs.

Abstract

The most important parameter in the coupling between solar wind and geomagnetic activity is the B_z -component of the interplanetary magnetic field (IMF). However, recent studies have shown that IMF B_y is an additional, independent driver of geomagnetic activity. We use here local geomagnetic indices from a large network of magnetic stations to study how IMF B_y affects geomagnetic activity at different latitudes for all solar wind and, separately during coronal mass ejections (CMEs). We show that geomagnetic activity, for all solar wind, is 20% stronger for $B_y > 0$ than for $B_y < 0$ at subauroral latitudes of about 60° corrected geomagnetic (CGM) latitude. During CMEs, the B_y -effect is larger, about 40%, at slightly lower latitudes of about 57° (CGM) latitude. These results highlight the importance of the IMF B_y -component for space weather at different latitudes and must be taken into account in space weather modeling.

1 Introduction

Geomagnetic activity, the short-term variability of the Earth's magnetic field, is caused by the interaction of solar wind and the Earth's magnetic field. The strongest magnetic disturbances on ground are due to auroral electrojets that are located at about 70° of corrected geomagnetic (CGM) latitude during average solar wind conditions. Severe space weather effects occur especially during geomagnetic storms, when the auroral region expands to subauroral or even lower latitudes. Extensive areas of infrastructure are then exposed to strong magnetic disturbances caused by the auroral electrojets, as for example in 1989, when a major blackout occurred in Quebec, Canada [Bolduc, 2002].

Detailed understanding of the relation between solar wind and geomagnetic activity is important for space weather research and effects. It is well known that the strongest levels of solar wind driving occur during the Earth-passage of coronal mass ejections (CMEs) [Gosling *et al.*, 1991; Gopalswamy *et al.*, 2005; Borovsky and Denton, 2006; Zhang *et al.*, 2007]. Coronal mass ejections observed at 1 AU often exhibit a magnetic cloud (MC) structure with several distinguishing features, including a smooth rotation of the magnetic field and a low plasma density and pressure [Burlaga, 1988; Zurbuchen and Richardson, 2006]. Magnetic clouds moving faster than the magnetosonic speed generate shocks and turbulent sheath regions which typically have highly variable magnetic fields and

a high plasma density [Kilpua *et al.*, 2013] and are also strong drivers of geomagnetic activity [Huttunen *et al.*, 2002; Yermolaev *et al.*, 2012].

The most critical solar wind parameter for geomagnetic activity is the B_z -component (measured in GSM coordinate system) of the interplanetary magnetic field (IMF), controlling reconnection rate in the dayside magnetopause. Both analytic work [Sonnerup, 1974] and MHD simulations [Fedder *et al.*, 1991; Laitinen *et al.*, 2007] have shown that also IMF B_y -component affects the reconnection rate. The IMF dependence of geomagnetic activity is often approximated by different coupling functions, such as the Newell universal coupling function [Newell *et al.*, 2007]

$$d\Phi_{MP}/dt = v^{4/3} B_T^{2/3} \sin^{8/3}(\theta/2), \quad (1)$$

where v is solar wind speed, $B_T = \sqrt{B_z^2 + B_y^2}$ and $\theta = \arctan(B_y/B_z)$ is the so-called IMF clock angle. In the Newell function $d\Phi_{MP}/dt$ (and in all other common coupling functions) the effect of B_y is symmetric, that is, changing the sign of B_y does not change the value of $d\Phi_{MP}/dt$. However, recent studies by Friis-Christensen *et al.* [2017] and Smith *et al.* [2017] showed that the AL -index (measuring the westward auroral electrojet) is considerably stronger for $B_y > 0$ than for $B_y < 0$ in Northern Hemisphere (NH) winter. Note that this *explicit* B_y -dependency is not due to the Russell-McPherron (RMP) effect [Russell and McPherron, 1973], which maximizes in April and October, leading to a more negative B_z even around northern winter (summer) solstice for $B_y < 0$ ($B_y > 0$). Holappa and Mursula [2018] quantified this explicit B_y -effect to the westward electrojet in both hemispheres by removing the influence of the RMP effect, and showed that the AL -index is about 40-50% stronger for $B_y > 0$ than for $B_y < 0$ around NH winter solstice. Even when averaged over all seasons and all solar wind data, AL -index is still about 12% stronger for $B_y > 0$ than for $B_y < 0$. Holappa and Mursula [2018] also showed that the B_y -effect works oppositely the Southern Hemisphere, where $B_y < 0$ yields to higher geomagnetic activity in local winter.

The exact physical mechanism of the explicit B_y -effect is still unknown. Radar observations have shown that IMF B_y affects the shape of the ionospheric convection patterns [Ruohoniemi and Greenwald, 2005; Pettigrew *et al.*, 2010]. Recently, Thomas and Shepherd [2018] showed that for a given value of solar wind convective electric field, the cross-polar cap potential (measuring the strength of ionospheric convection) is greater for $B_y > 0$ than for $B_y < 0$ in winter, which is consistent with the above results based

on geomagnetic activity. *Holappa and Mursula* [2018] showed that the B_y -effect in NH maximizes at 5 UT, that is, when the Earth’s dipole axis points towards midnight and the NH ionosphere is maximally in darkness. The combined UT/seasonal variation of the B_y -effect indicates that the B_y -effect is most effective under low ionospheric conductivity. This is further supported by the fact that the B_y -effect in the SH maximizes in local winter. However, the B_y -dependencies in SH and NH are opposite: geomagnetic activity in the SH is higher for $B_y < 0$ than for $B_y > 0$.

From space weather perspective, it is crucial to quantify the significance of the B_y -effect at different latitudes. This has not yet been done in previous studies, which are all based on global geomagnetic indices. This paper studies how the B_y -effect modulates geomagnetic activity at different latitudes by using local geomagnetic indices from a large network of magnetic stations. We will focus on periods of strong CME-driven geomagnetic activity. This paper is organized as follows. In Section 2 we introduce the database of CMEs and other solar wind data, as well as geomagnetic indices used in this paper. In Section 3 we study the latitudinal distribution of geomagnetic activity during CMEs. In Section 4 we study the effect of B_y to local geomagnetic activity at different latitudes. In Section 5 we study the seasonal variation of the B_y -effect. Finally, we give our conclusions in Section 6.

2 Data

In this paper we use hourly averages of solar wind and IMF parameters measured in the GSM coordinate system from the OMNI2 database (<http://omniweb.gsfc.nasa.gov/>). We also use a list of 164 CMEs (magnetic clouds and associated sheath regions) identified from solar wind measurements by the Wind satellite at 1 AU in 1995-2015 [*Gopalswamy et al.*, 2015]. The primary identification criteria for MCs are low proton temperature and/or low plasma beta and smooth rotation of IMF. (For a more detailed discussion on CME observations, see *Gopalswamy et al.*, 2015).

We use local measurements of geomagnetic activity from 44 stations in 1995-2016. The list of stations and their coordinates are given in Table 1. For all these stations we calculate their A_h -indices [*Mursula and Martini*, 2007] measuring local geomagnetic activity. A_h indices are analogous to local K/A_k -indices, measuring the range of variation of the local horizontal magnetic field in three-hour intervals after removing the regular

diurnal variation due to the solar quiet (Sq) currents in the ionosphere. *Mursula and Martini* [2007] showed that the local A_h -indices correlate very well with the local K/A_k -indices, which are known to be good proxies for local GIC amplitudes [*Viljanen et al.*, 2006]. Thus, the A_h -indices provide a well-suited database for studying the significance and space weather impact of the B_y -effect at different latitudes.

3 Latitudinal distribution of geomagnetic activity driven by CMEs

Figure 1a shows the average values of A_h indices during the 164 CMEs ($\langle A_h(CME) \rangle$) and for all solar wind data in 1995-2016 ($\langle A_h(all\ SW) \rangle$) as a function of the corrected geomagnetic latitude of the station. Figure 1a verifies the well-known fact that geomagnetic activity is almost an order-of-magnitude stronger in the auroral region at about $65^\circ - 70^\circ$ than at low latitudes. While $\langle A_h(all\ SW) \rangle$ shows a fairly sharp peak at 70° , $\langle A_h(CME) \rangle$ exhibits a clear broadening of the peak towards lower latitudes, with almost a plateau formed at about $64^\circ - 68^\circ$.

When averaged over all stations, $\langle A_h(CME) \rangle$ is 77% greater than $\langle A_h(all\ SW) \rangle$. However, there are latitudinal differences in the relative increase of geomagnetic activity. This can be better seen in Figure 1b, which shows the ratio

$$R^{CME} = \frac{\langle A_h(CME) \rangle}{\langle A_h(all\ SW) \rangle} \quad (2)$$

as a function of corrected geomagnetic latitude. While the ratio R^{CME} is almost a constant (about 2) at low and mid-latitudes, it reaches a peak of about 3.5 at subauroral latitudes (around 60°) and shows a minimum of about 1.5 in auroral latitudes (around 70°). This is due to expansion of the auroral oval to lower latitudes due to strong driving by CMEs [*Borovsky and Denton*, 2006; *Holappa et al.*, 2014]. While geomagnetic activity increases at all latitudes during CMEs, the expansion of the auroral oval brings subauroral stations closer to the auroral electrojets, leading to a strong relative increase of activity at subauroral latitudes.

Expansion of the auroral oval during CMEs is further studied in Figure 1b, which shows the normalized ratio

$$R_n^{CME} = R^{CME} \cdot \left(\frac{\langle d\Phi_{MP}/dt(CME) \rangle}{\langle d\Phi_{MP}/dt(all\ SW) \rangle} \right)^{-1} = \frac{\langle A_h(CME) \rangle}{\langle A_h(all\ SW) \rangle} \cdot \left(\frac{\langle d\Phi_{MP}/dt(CME) \rangle}{\langle d\Phi_{MP}/dt(all\ SW) \rangle} \right)^{-1}. \quad (3)$$

The ratio R_n^{CME} is close to one at low and mid-latitudes. Thus, the relative increase of the solar wind driving (quantified by the ratio $\langle d\Phi_{MP}/dt(CME) \rangle / \langle d\Phi_{MP}/dt(all\ SW) \rangle$)

Table 1. Stations and their corrected geomagnetic (CGM) and geographic (GG) coordinates.

Stations are ordered according to their CGM latitudes.

#	Code	CGMlat	CGMlong	GGlat	GGlong	#	Code	CGMlat	CGMlong	GGlat	GGlong
1	ABG	10.37	146.54	18.64	72.87	23	WNG	49.96	86.38	53.74	9.07
2	MBO	19.90	57.82	14.38	-16.97	24	HLP	50.76	94.87	54.61	18.82
3	HON	21.28	-89.48	21.32	-158.00	25	NVS	50.84	156.56	54.85	83.23
4	KNY	24.87	-156.48	31.42	130.88	26	ESK	52.57	77.04	55.32	-3.20
5	SJG	28.31	6.57	18.38	-66.12	27	VIC	53.67	-62.36	48.52	-123.42
6	KAK	29.47	-147.48	36.23	140.18	28	NEW	54.72	-54.80	48.27	-117.12
7	BMT	34.75	-170.52	40.30	116.20	29	NUR	57.04	102.00	60.51	24.66
8	MMB	37.28	-143.77	43.91	144.19	30	LER	57.87	80.49	60.13	-1.18
9	TUC	39.81	-44.07	32.25	-110.83	31	SIT	59.67	-78.19	57.05	-135.34
10	NCK	42.78	91.49	47.63	16.72	32	MEA	61.67	-52.10	54.62	-113.35
11	PAG	42.81	98.63	47.48	24.18	33	SOD	64.09	107.04	67.37	26.63
12	HRB	43.08	92.79	47.87	18.19	34	LRV	64.64	66.11	64.18	-21.70
13	CLF	43.32	79.20	48.02	2.27	35	ABK	65.44	101.72	68.36	18.82
14	FUR	43.57	87.31	48.17	11.28	36	FCC	68.32	-25.96	58.79	-94.09
15	BDV	44.58	89.82	49.08	14.02	37	YKC	69.15	-57.04	62.48	-114.48
16	MAB	46.18	82.95	50.30	5.68	38	BRW	70.27	-106.53	71.30	-156.62
17	IRT	47.24	177.95	52.17	104.45	39	BLC	73.33	-30.33	64.33	-96.03
18	HAD	47.37	74.46	51.00	-4.48	40	HRN	74.34	108.24	77.00	15.55
19	BEL	47.65	96.08	51.84	20.79	41	GDH	75.05	38.41	69.25	-53.53
20	NGK	47.95	88.96	52.07	12.68	42	CBB	76.81	-47.90	69.12	-105.03
21	FRD	48.33	-1.09	38.21	-77.37	43	RES	82.76	-35.89	74.69	-94.89
22	BOU	48.66	-38.58	40.13	-105.23	44	THL	84.64	28.23	77.48	-69.17

explains the relative increase of geomagnetic activity at these latitudes. However, the ratio R_n^{CME} peaks at subauroral latitudes (with a maximum of about 1.8) and is slightly below one at auroral latitudes (with a minimum of 0.8). Thus, the expansion of the auroral oval during CMEs leads to stronger (weaker) relative increase of geomagnetic activity at subauroral (auroral) latitudes.

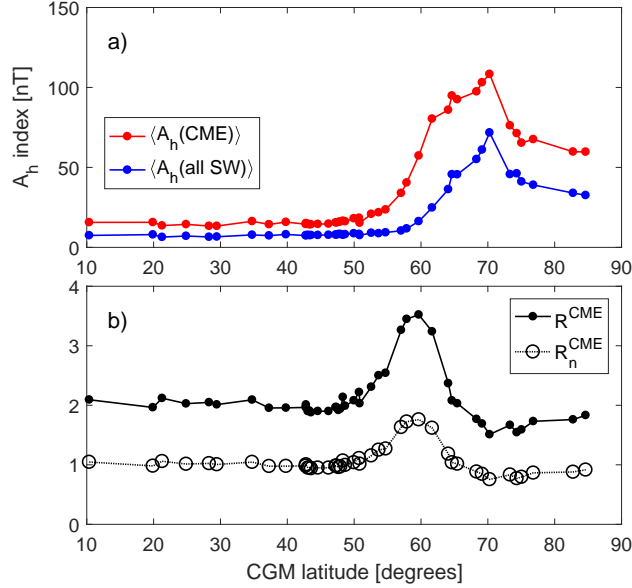


Figure 1. a) Latitudinal distribution of the average A_h -indices during CMEs ($\langle A_h(CME) \rangle$) and all solar wind ($\langle A_h(all SW) \rangle$). b) Latitudinal distributions of the ratio $R^{CME} = \langle A_h(CME) \rangle / \langle A_h(all SW) \rangle$ and the normalized ratio R_n^{CME} defined in Eq. (3).

4 Effect of IMF B_y at different latitudes

Figures 2a and 2b show the mean A_h indices for $B_y > 0$ and $B_y < 0$ for all solar wind and during CMEs, respectively. In Figure 2b the sign of B_y has only a rather small effect. When averaging over all data and all stations, $\langle A_h \rangle$ indices are only 7.6% stronger for $B_y > 0$ than for $B_y < 0$. This is smaller than the 12% B_y -effect to the AL -index found by *Holappa and Mursula* [2018]. A smaller B_y -effect is understandable because the AL -index measures the strength of the westward electrojet (located mainly in midnight and dawn sectors), while the A_h -indices also include the effect of the eastward electrojet (afternoon sector), which is not affected by B_y [*Holappa and Mursula*,

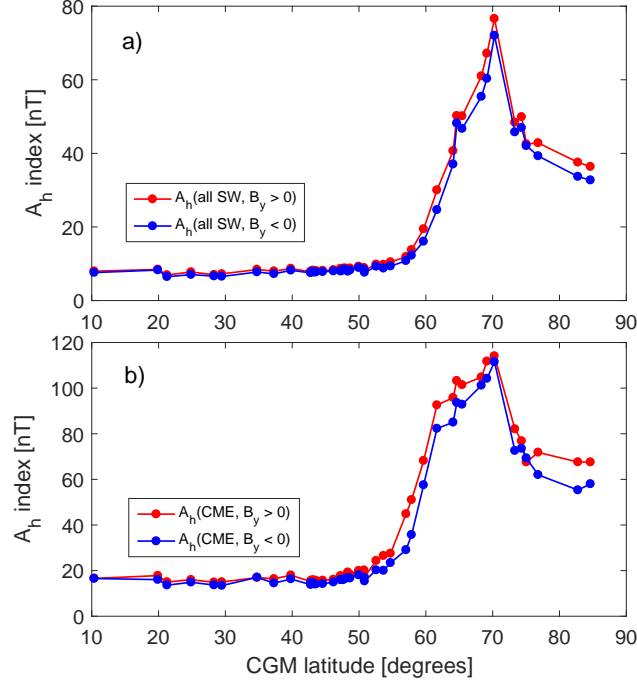


Figure 2. Latitudinal distribution of A_h -indices for IMF $B_y > 0$ and for $B < 0$ during a) all solar wind b) CMEs.

2018]. Interestingly, the B_y -effect is clearly stronger (12.4%) for CMEs (Fig. 2b) than for all solar wind, when averaged over all stations.

In order to rule out the possibility that the above B_y -effect is an artifact due to biased data selection, we calculate the probability distribution functions (PDF) of IMF B_z and $d\Phi_{MP}/dt$ for $B_y > 0$ and $B_y < 0$. Figures 3a and 3b show the PDFs of three-hour means of B_z for all solar wind and for CME events, respectively. Figure 3a shows that, when all solar wind data are included in the statistics, the distribution of B_z is virtually the same for $B_y > 0$ and $B_y < 0$. Moreover, Figure 3b shows that even for the rather modest number of 164 CME events of our sample, the distributions of B_z are almost equal for both signs of B_y . Figures 3c and 3d are similar to Figures 3a and 3b, but show the PDFs for three-hour means of $d\Phi_{MP}/dt$. Again, the distributions of $d\Phi_{MP}/dt$ are almost the same for $B_y > 0$ and $B_y < 0$. Thus, there are no significant statistical differences in solar wind driving, which could explain the higher response in geomagnetic activity for $B_y > 0$ than for $B_y < 0$.

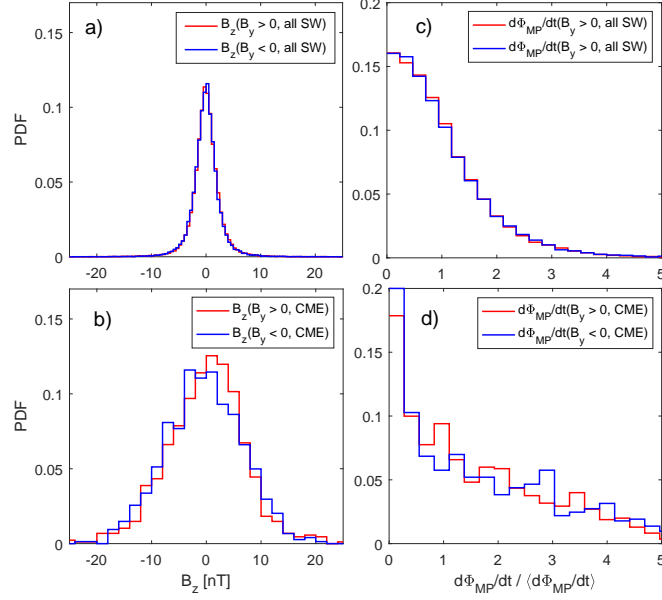


Figure 3. a-b) Probability density functions of IMF B_z in GSM coordinate system for CMEs and all solar wind. c-d) Probability density functions of the Newell universal coupling function $d\Phi_{MP}/dt$ in GSM coordinate system for CMEs and all solar wind.

The relative size of the B_y -effect to geomagnetic activity at different latitudes is better seen in Figures 4a and 4b, which show the normalized ratios

$$R_n^{+/-}(all\ SW) = \frac{\langle A_h(all\ SW, B_y > 0) \rangle}{\langle A_h(all\ SW, B_y < 0) \rangle} \cdot \left(\frac{\langle d\Phi_{MP}/dt(all\ SW, B_y > 0) \rangle}{\langle d\Phi_{MP}/dt(all\ SW, B_y < 0) \rangle} \right)^{-1} \quad (4)$$

and

$$R_n^{+/-}(CME) = \frac{\langle A_h(CME, B_y > 0) \rangle}{\langle A_h(CME, B_y < 0) \rangle} \cdot \left(\frac{\langle d\Phi_{MP}/dt(CME, B_y > 0) \rangle}{\langle d\Phi_{MP}/dt(CME, B_y < 0) \rangle} \right)^{-1}, \quad (5)$$

respectively. The most striking feature in Figure 4b is the high peak in $R_n^{+/-}(CME)$ ratio of about 1.5 peaking at subauroral latitudes of about 57° . The peak of $R_n^{+/-}(all\ SW)$ in Fig. 4a is also found at subauroral latitudes at about 60° , but the peak value (1.2) is considerably lower than for $R_n^{+/-}(CME)$. Both $R_n^{+/-}(CME)$ and $R_n^{+/-}(all\ SW)$ exhibit some irregularities in their latitudinal distributions, probably due to longitudinal dependence of the B_y -effect. (We leave the detailed analysis of longitudinal dependence out of this paper.) At latitudes below 45° both $R_n^{+/-}(CME)$ and $R_n^{+/-}(all\ SW)$ are mostly slightly greater than one. Interestingly, both $R_n^{+/-}(CME)$ and $R_n^{+/-}(all\ SW)$ are only slightly greater than one at auroral latitudes (around 70°). This indicates that the auroral electrojets are extended further to subauroral latitudes for $B_y > 0$ than for $B_y < 0$, decreasing the relative B_y -effect in auroral latitudes. Figures 4a and 4b also include

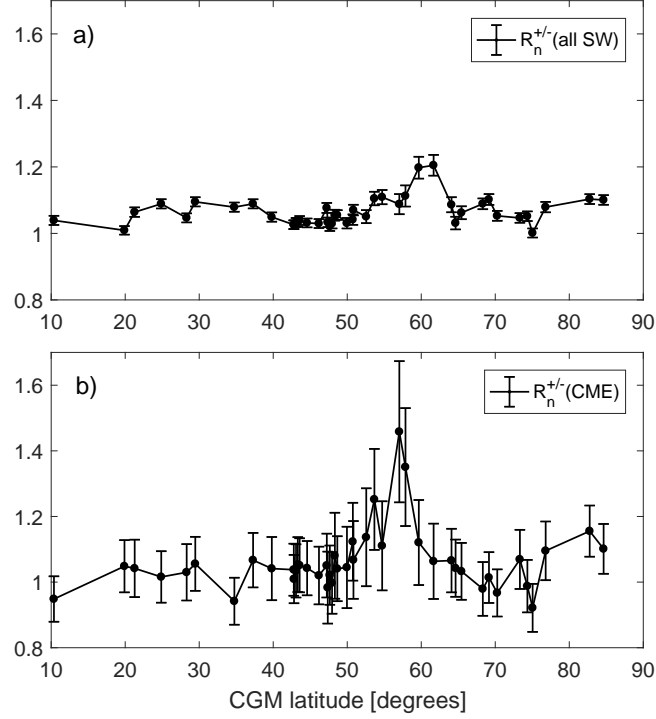


Figure 4. Normalized ratios $R_n^{+/-}(\text{all SW})$ (a) $R_n^{+/-}(\text{CME})$ (b) defined in Equations (4-5).

The vertical bars show the standard errors.

the standard errors of the two ratios, calculated by the formula [Kendall *et al.*, 1994]

$$\sigma(R_n^{+/-}) \approx \frac{\langle A_h(B_y > 0) \rangle}{\langle A_h(B_y < 0) \rangle} \sqrt{\frac{\sigma(\langle A_h(B_y > 0) \rangle)^2}{\langle A_h(B_y > 0) \rangle^2} + \frac{\sigma(\langle A_h(B_y < 0) \rangle)^2}{\langle A_h(B_y < 0) \rangle^2}} \cdot \left(\frac{\langle d\Phi_{MP}/dt(B_y > 0) \rangle}{\langle d\Phi_{MP}/dt(B_y < 0) \rangle} \right)^{-1}, \quad (6)$$

where $\sigma(\cdot)$ denotes the standard error. The relatively small sample size of 164 CMEs leads to considerably larger errors for CMEs than for all SW.

In order to further verify the robustness of the above results we have plotted in Figure 5a the ratio

$$R_n^{+/-}(\text{all SW}, B_z < -5) = \frac{\langle A_h(B_z < -5, B_y > 0) \rangle}{\langle A_h(B_z < -5, B_y < 0) \rangle} \cdot \left(\frac{\langle d\Phi_{MP}/dt(\text{all SW}, B_y > 0) \rangle}{\langle d\Phi_{MP}/dt(\text{all SW}, B_y < 0) \rangle} \right)^{-1} \quad (7)$$

based on all 3-hour intervals solar wind data in 1995-2016 for which the three-hourly averaged $B_z < -5$ nT. While this requirement does not exclusively identify CMEs from solar wind data, it ensures that solar wind driving is quite intense for a considerable time. Only 3.2% of solar wind measurements meet this criterion (cf. Figure 3a). Because persistent strongly negative B_z periods are commonly found within CMEs, but not, e.g., dur-

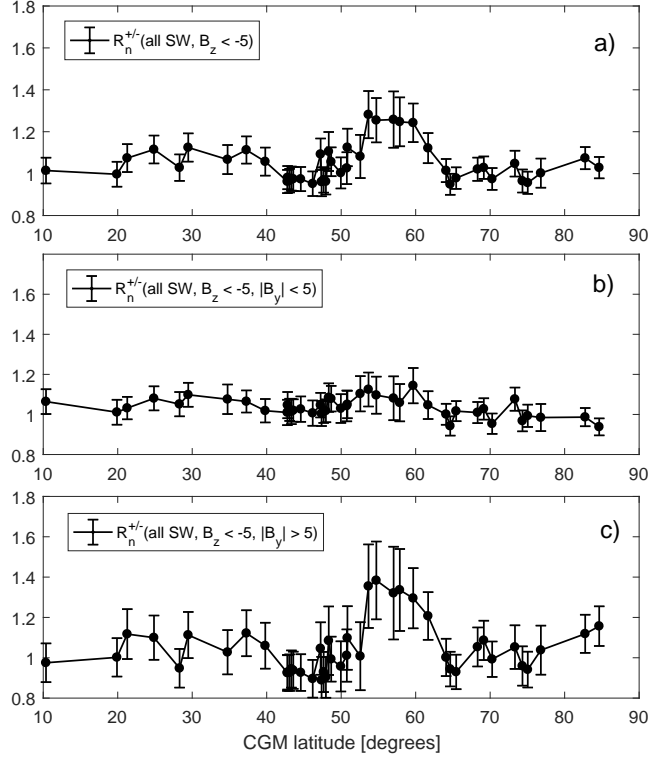


Figure 5. a) Ratio $R_n^{+/-}$ (all SW, $B_z < -5$) defined in Eq. (7) b) ratio $R_n^{+/-}$ (all SW, $B_z < -5$, $|B_y| < 5$) c) ratio $R_n^{+/-}$ (all SW, $B_z < -5$, $|B_y| > 5$). Vertical bars denote the standard errors.

ing CIRs/HSSs [Tsurutani *et al.*, 1995; Yermolaev *et al.*, 2012], the non-CME solar wind structures contribute to Figure 5 quite little. Even though only a small fraction of all solar wind data is used in Figure 5, it is based on significantly larger statistics (1256 3-hr bins) than the results based on selected CME events (Figs. 2b, 4b and 4b).

Figure 5a shows that subauroral geomagnetic activity between $54^\circ - 59^\circ$ is significantly greater for $B_y > 0$ than for $B_y < 0$ during strong solar wind driving. The peak of the ratio $R_n^{+/-}$ (all SW, $B_z < -5$) is about 1.3, in a close agreement with $R_n^{+/-}$ (CME) in Figure 4. However, the peak of $R_n^{+/-}$ (all SW, $B_z < -5$) extends to even lower latitudes than the peak of $R_n^{+/-}$ (CME). This indicates that the average level of geomagnetic activity is stronger under the condition $B_z < -5$ nT than during CMEs, which include strongly negative but also strongly positive values of B_z .

In the above analysis we have only quantified the effect of the sign of B_y , without considering the amplitude $|B_y|$. Figures 5b and 5c repeat the analysis of Figure 5a, im-

posing additional criterions: $|B_y| < 5$ nT and $|B_y| > 5$ nT, respectively. The ratio $R_n^{+/-}$ (*all SW*, $B_z < -5$, $|B_y| < 5$) in Fig. Fig. 5b is only slightly above one at most latitudes while the ratio $R_n^{+/-}$ (*all SW*, $B_z < -5$, $|B_y| > 5$) reaches a maximum of about 1.4 between $54^\circ - 59^\circ$. This indicates that the B_y -effect is only significant for rather strong values of B_y . Interestingly, Figures 5a and 5c show a local minimum at mid-latitudes at about $43^\circ - 46^\circ$, where both ratios $R^{+/-}$ are close to one (within statistical error).

Figure 5 highlights the importance of the B_y -effect for subauroral geomagnetic activity. Because the amplitude of IMF B_y can be much larger than 5 nT, especially within CMEs, the B_y -effect can be even more important than in Figure 5c in extreme cases.

5 Seasonal variation

In the above analysis we have studied the B_y -effect by averaging over all seasons. However, as earlier studies [Fris-Christensen *et al.*, 2017; Smith *et al.*, 2017; Holappa and Mursula, 2018] have shown, the B_y -effect is seasonally varying, maximizing in winter. Figure 6 shows the ratio $R_n^{+/-}$ (*all SW*, $-3 < B_z < 0$) separately for winter and summer (± 30 days around winter and summer solstices, respectively). To have sufficient statistics, we have selected only periods of modest solar wind driving: -3 nT $< B_z < 0$. Figure 6 shows that subauroral geomagnetic activity at about $57^\circ - 61^\circ$ is stronger for $B_y > 0$ than for $B_y < 0$ by a factor of 1.4-1.9 in winter. The peak of $R_n^{+/-}$ (*all SW*, $-3 < B_z < 0$) is at higher latitude (61°) than in Figures 5a and 5b. Note that for auroral latitudes, the ratio $R_n^{+/-}$ of Figure 6 gives roughly the same value of about 1.4 as earlier when using the auroral AL -index [Holappa and Mursula, 2018]. Figure 6 also shows that the maximum B_y -effect is not at the auroral latitudes. In summer the ratio $R_n^{+/-}$ (*all SW*, $-3 < B_z < 0$) is slightly below one at most latitudes, and it reaches a minimum of about 0.8 around 65° . This is in agreement with [Holappa and Mursula, 2018] who found that the AL -index (measured between 60° and 70°) is about 20% weaker for $B_y > 0$ than for $B_y < 0$ around summer solstice.

6 Discussion and conclusions

In this paper we have studied the latitudinal distribution of the recently found explicit IMF B_y -dependence of geomagnetic activity for all solar wind and, separately, during coronal mass ejections. We find that the IMF B_y -component modulates geomagnetic activity for all solar wind and even more during CMEs, especially at subauroral latitudes.

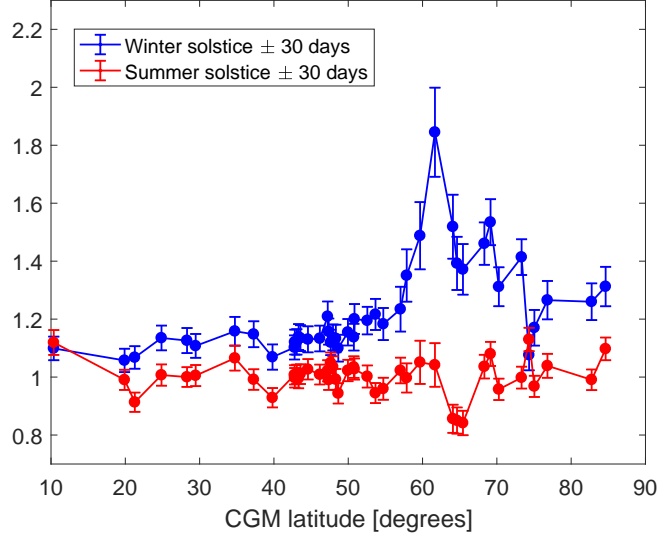


Figure 6. Ratio $R_n^{+/-}$ (all SW, $-3 < B_z < 0$) calculated for winter and summer (± 30 days around winter and summer solstices, respectively)

During CMEs the B_y -effect maximizes at 59° of corrected geomagnetic latitude, where local geomagnetic activity is about 40% stronger for $B_y > 0$ than for $B_y < 0$. The B_y -effect is relatively much stronger at subauroral latitudes than auroral latitudes, where it is only about 10%. This indicates that the auroral electrojets are latitudinally more extensive for $B_y > 0$ than for $B_y < 0$.

We also showed that a similar (about 30%) B_y -effect at subauroral latitudes is observed for periods when the 3-hr average of IMF $B_z < -5$ nT. The size of the B_y -effect is even stronger (about 40%) if, in addition to $B_z < -5$ nT, we require B_y to be large ($|B_y| > 5$ nT).

The physical mechanism of the explicit B_y -dependence is not yet known. *Friis-Christensen et al.* [2017] showed that the B_y -effect mainly operates in the night sector and suggested that IMF B_y modulates the strength of the substorm current wedge. This is supported by *Holappa and Mursula* [2018] who showed that the B_y -effect modulates the AL -index (which is strongly affected by the substorm current wedge), but not the AU -index, which measures the eastward electrojet (not connected to the substorm current wedge). Under this assumption, our results suggest that the substorm current wedge extends to lower latitudes for $B_y > 0$ than for $B_y < 0$.

Earlier studies have also shown that the B_y -effect exhibits a strong seasonal variation, maximizing in winter [Smith *et al.*, 2017; Holappa and Mursula, 2018]. In this paper we showed that the B_y -effect is important in winter at all latitudes. We find at least a 10-20% effect at all latitudes, with a maximum at subauroral latitudes, where $B_y > 0$ yields nearly twice stronger geomagnetic activity than $B_y < 0$. The large winter B_y -effect supports the earlier finding that the B_y -effect maximizes when the ionosphere is maximally in darkness [Holappa and Mursula, 2018]. Thus, the underlying mechanism of the B_y -effect is probably most efficient when the ionospheric conductivity is lowest. We also showed that during summer solstice the only significant B_y -effect is found at auroral latitudes of about 65° , where geomagnetic activity is about 20% weaker for $B_y > 0$ than for $B_y < 0$.

The results of this paper highlight the importance of the explicit IMF B_y -effect for understanding and predicting space weather effects at different latitudes, in particular during CMEs.

Acknowledgments

We acknowledge the financial support by the Academy of Finland to the ReSoLVE Centre of Excellence (project no. 272157). The solar wind data were downloaded from the OMNI2 database (<http://omniweb.gsfc.nasa.gov/>). Magnetometer data were downloaded from World Data Center, Edinburgh (<http://www.wdc.bgs.ac.uk/>).

References

- Bolduc, L. (2002), GIC observations and studies in the Hydro-Québec power system, *J. Atm. Sol.-Terr. Phys.*, *64*(16), 1793–1802.
- Borovsky, J. E., and M. H. Denton (2006), Differences between CME-driven storms and CIR-driven storms, *J. Geophys. Res.*, *111*, A07S08, doi:10.1029/2005JA011447.
- Burlaga, L. F. (1988), Magnetic clouds and force-free fields with constant alpha, *J. Geophys. Res.*, *93*, 7217–7224, doi:10.1029/JA093iA07p07217.
- Fedder, J. A., C. M. Mobarry, and J. G. Lyon (1991), Reconnection voltage as a function of imf clock angle, *Geophys. Res. Lett.*, *18*(6), 1047–1050.

- Friis-Christensen, E., C. C. Finlay, M. Hesse, and K. M. Laundal (2017), Magnetic Field Perturbations from Currents in the Dark Polar Regions During Quiet Geomagnetic Conditions, *Space Sci. Rev.*, *206*(1-4), 281–297.
- Gopalswamy, N., S. Yashiro, G. Michalek, H. Xie, R. P. Lepping, and R. A. Howard (2005), Solar source of the largest geomagnetic storm of cycle 23, *Geophys. Res. Lett.*, *32*(12).
- Gopalswamy, N., S. Yashiro, H. Xie, S. Akiyama, and P. Mäkelä (2015), Properties and geoeffectiveness of magnetic clouds during solar cycles 23 and 24, *J. Geophys. Res.*, *120*(11), 9221–9245.
- Gosling, J. T., D. J. McComas, J. L. Phillips, and S. J. Bame (1991), Geomagnetic activity associated with earth passage of interplanetary shock disturbances and coronal mass ejections, *J. Geophys. Res.*, *96*, 7831–7839, doi:10.1029/91JA00316.
- Holappa, L., and K. Mursula (2018), Explicit IMF B_y -dependence in high-latitude geomagnetic activity, *J. Geophys. Res.*, *123*, 4728–4740, doi:10.1029/2018JA025517.
- Holappa, L., K. Mursula, T. Asikainen, and I. G. Richardson (2014), Annual fractions of high-speed streams from principal component analysis of local geomagnetic activity, *J. Geophys. Res.*, *119*(6), 4544–4555, doi:10.1002/2014JA019958.
- Huttunen, E. K. J., H. E. J. Koskinen, and R. Schwenn (2002), Variability of magnetospheric storms driven by different solar wind perturbations, *J. Geophys. Res.*, *107*(A7), SMP 20–1–SMP 20–8, doi:10.1029/2001JA900171.
- Kendall, M., A. Stuart, and J. Ord (1994), *Kendall's advanced theory of statistics. Vol. 1: Distribution theory*, Arnold, London.
- Kilpua, E. K. J., H. Hietala, H. E. J. Koskinen, D. Fontaine, and L. Turc (2013), Magnetic field and dynamic pressure ulf fluctuations in coronal-mass-ejection-driven sheath regions, *Ann. Geophys.*, *31*(9), 1559–1567, doi:10.5194/angeo-31-1559-2013.
- Laitinen, T. V., M. Palmroth, T. I. Pulkkinen, P. Janhunen, and H. E. J. Koskinen (2007), Continuous reconnection line and pressure-dependent energy conversion on the magnetopause in a global mhd model, *J. Geophys. Res.*, *112*(A11).
- Mursula, K., and D. Martini (2007), New indices of geomagnetic activity at test: Comparing the correlation of the analogue a_k index with the digital A_h and IHV indices at the Sodankylä station, *Adv. Space Res.*, *40*, 1105–1111, doi:

- 10.1016/j.asr.2007.06.067.
- Newell, P. T., T. Sotirelis, K. Liou, C.-I. Meng, and F. J. Rich (2007), A nearly universal solar wind-magnetosphere coupling function inferred from 10 magnetospheric state variables, *J. Geophys. Res.*, *112*(A1).
- Pettigrew, E. D., S. G. Shepherd, and J. M. Ruohoniemi (2010), Climatological patterns of high-latitude convection in the Northern and Southern hemispheres: Dipole tilt dependencies and interhemispheric comparisons, *J. Geophys. Res.*, *115*(A7), A07305, doi:10.1029/2009JA014956, a07305.
- Ruohoniemi, J. M., and R. A. Greenwald (2005), Dependencies of high-latitude plasma convection: Consideration of interplanetary magnetic field, seasonal, and universal time factors in statistical patterns, *J. Geophys. Res.*, *110*(A9).
- Russell, C. T., and R. L. McPherron (1973), Semiannual variation of geomagnetic activity, *J. Geophys. Res.*, *78*(1), 92–108.
- Smith, A. R. A., C. D. Beggan, S. Macmillan, and K. A. Whaler (2017), Climatology of the auroral electrojets derived from the along-track gradient of magnetic field intensity measured by POGO, Magsat, CHAMP, and Swarm, *Space Weather*, *15*(10), 1257–1269, doi:10.1002/2017SW001675, 2017SW001675.
- Sonnerup, B. U. O. (1974), Magnetopause reconnection rate, *J. Geophys. Res.*, *79*(10), 1546–1549, doi:10.1029/JA079i010p01546.
- Thomas, E. G., and S. G. Shepherd (2018), Statistical patterns of ionospheric convection derived from mid-latitude, high-latitude, and polar SuperDARN HF radar observations, *J. Geophys. Res.*, *123*(4), 3196–3216.
- Tsurutani, B. T., W. D. Gonzalez, A. L. C. Gonzalez, F. Tang, J. K. Arballo, and M. Okada (1995), Interplanetary origin of geomagnetic activity in the declining phase of the solar cycle, *J. Geophys. Res.*, *100*, 21,717–21,734, doi:10.1029/95JA01476.
- Viljanen, A., A. Pulkkinen, R. Pirjola, K. Pajunpää, P. Posio, and A. Koistinen (2006), Recordings of geomagnetically induced currents and a nowcasting service of the Finnish natural gas pipeline system, *Space Weather*, *4*(10).
- Yermolaev, Y. I., N. S. Nikolaeva, I. G. Lodkina, and M. Y. Yermolaev (2012), Geoeffectiveness and efficiency of cir, sheath, and icme in generation of magnetic storms, *J. Geophys. Res.*, *117*(A9).

- Zhang, J., I. G. Richardson, D. F. Webb, N. Gopalswamy, E. Huttunen, J. C. Kasper, N. V. Nitta, W. Poomvises, B. J. Thompson, C.-C. Wu, S. Yashiro, and A. N. Zhukov (2007), Solar and interplanetary sources of major geomagnetic storms ($Dst < -100$ nT) during 1996-2005, *J. Geophys. Res.*, *112*, A10,102, doi:10.1029/2007JA012321.
- Zurbuchen, T. H., and I. G. Richardson (2006), In-Situ Solar Wind and Magnetic Field Signatures of Interplanetary Coronal Mass Ejections, *Space Sci. Rev.*, *123*, 31–43, doi:10.1007/s11214-006-9010-4.